Magnetic Resonance Imaging 56 (2019) 110–118

Contents lists available at ScienceDirect

Magnetic Resonance Imaging

journal homepage: www.elsevier.com/locate/mri

Original contribution

Capturing complexity of the diffusion-weighted MR signal decay

Richard L. Magin[a,*], M. Muge Karaman[b], Matt G. Hall[c], Wenzhen Zhu[d], Xiaohong Joe Zhou[e]

[a] Richard and Loan Hill Department of Bioengineering, University of Illinois at Chicago, Chicago, IL 60607, USA
[b] Center for Magnetic Resonance Research, University of Illinois College of Medicine, Chicago, IL 60602, USA
[c] Institute of Child Health, University College London, London WC1N 1EH, United Kingdom
[d] Department of Radiology, Tongji Hospital, Huazhong University of Science and Technology, Wuhan, Hubei, China
[e] Center for Magnetic Resonance Research and Department of Radiology, University of Illinois College of Medicine, Chicago, IL 60602, USA

ARTICLE INFO

Keywords:
Magnetic resonance imaging
Apparent diffusion coefficient
Anomalous diffusion
Brain cancer
High b-value

ABSTRACT

Diffusion-weighted MRI (dMRI) is a key component of clinical radiology. When analyzing diffusion-weighted images, radiologists often seek to infer microscopic tissue structure through measurements of the diffusion coefficient, D_0 (mm^2/s). This multi-scale problem is framed by the creation of diffusion models of signal decay based on physical laws, histological structure, and biophysical constraints. The purpose of this paper is to simplify the model building process by focusing on the observed decay in the effective diffusion coefficient as a function of diffusion weighting (b-value), $D(b)$, that is often observed in complex biological tissues. We call this approach the varying diffusion curvature (VDC) model. Since this is a heuristic model, the exact functional form of this decay is not important, so here we examine a simple exponential function, $D(b) = D_0 exp(-bD_1)$, where D_0 and D_1 capture aspects of hindered and restricted diffusion, respectively. As an example of the potential of the VDC model, we applied it to dMRI data collected from normal and diseased human brain tissue using Stejskal-Tanner diffusion gradient pulses. In order to illustrate the connection between D_0 and D_1 and the sub-voxel structure we also analyzed dMRI data from families of Sephadex beads selected with increasing tortuosity. Finally, we applied the VDC model to dMRI simulations of nested muscle fiber phantoms whose permeability, atrophy, and fiber size distribution could be changed. These results demonstrate that the VDC model is sensitive to sub-voxel tissue structure and composition (porosity, tortuosity, and permeability), hence can capture tissue complexity in a manner that could be easily applied in clinical dMRI.

1. Introduction

Diffusion-weighted magnetic resonance imaging (dMRI) uses motion sensitizing gradients to describe the movement of water molecules in, around, and through cells. For the radiologist, dMRI provides tissue contrast for identifying stroke [1], delineating cancer [2–4] and characterizing a host of other diseases [1]. For the patient, dMRI furnishes visual reassurance that their condition has been identified and quantified. For the researcher, dMRI offers an expanding toolbox for tissue assessment benefiting from steady advances in hardware (RF, gradient coils, high B_0 magnets) and sub-voxel tissue models (e.g., diffusion kurtosis [5], random walks with barriers [6], neurite orientation dispersion and density imaging [7], and composite hindered and restricted model of diffusion [8]). Using fast and efficient pulse sequences, dMRI, as it is applied in most clinics today, can quickly identify defects or damage to soft tissue with high resolution and contrast. dMRI is complementary to T_1 and T_2 relaxation contrast (which relies on molecular dynamics and dipole interactions) due to its sensitivity to the translational diffusion of water at the micron length scale of cells. Hence, dMRI, can identify tissue changes in intracellular, extracellular, and vascular compartments via the selective reduction in signal intensity at high, intermediate, and low b-values (i.e., diffusion weighting).

The mobility of water in biological tissues is not completely random; but is hindered and restricted by cellular and sub-cellular tissue structure, as well as by the extracellular matrix of proteoglycans and fibrous proteins. In dMRI, the response of water molecules to diffusion encodes (through phase incoherence) information about the local arrangement, composition, and membrane permeability of different tissue structures.

Abbreviations: dMRI, diffusion-weighted magnetic resonance imaging; VDC, varying diffusion curvature; RF, radiofrequency; TR, repetition time; TE, echo time; PGSE, pulse gradient spin-echo; OCSE, oscillating gradient spin-echo; ADC, apparent diffusion coefficient; K, excess kurtosis; FOV, field of view; CSF, cerebral spinal fluid; WM, white matter; GM, gray matter; DMD, Duchenne muscular dystrophy; Mdx, mouse model of Duchenne muscular dystrophy; SNR, signal-to-noise ratio

* Corresponding author at: Richard L. Magin, Richard and Loan Hill Department of Bioengineering, University of Illinois at Chicago, SEO Room 218 (MC 063), 851 South Morgan St., Chicago, IL 60607, USA.
E-mail address: rmagin@uic.edu (R.L. Magin).

https://doi.org/10.1016/j.mri.2018.09.034
Received 19 July 2018; Received in revised form 26 September 2018; Accepted 28 September 2018

As such, the overall goal of diffusion imaging is to establish how the microstructural and physiological parameters relate to the diffusion-weighted MR signal. This requires mathematical models whose parameters reflect features (e.g., porosity, tortuosity, heterogeneity, surface to volume ratio, permeability) of the cellular organization of tissue and its composition. The tissue characterizing parameters extracted from the diffusion-weighted MR signal also depend on the formulation of the mathematical models (linear, non-linear, integer, or fractional order) used to describe the signal. Current practice assumes Gaussian diffusion conditions that predict an exponential function model of the signal decay expressed in terms of the apparent diffusion coefficient (ADC, mm^2/s).

Given the heterogeneous nature of biological tissues – in health and disease – with their varying structural heterogeneity and complexity, it is not surprising that diffusion is not always Gaussian, hence, many diffusion models have been suggested by the porous media, imaging and biophysics communities, to model diffusion phenomenon in cells, in tissues, and in organs (e.g., hindered, restricted, isotropic, anisotropic, and normal or anomalous). Such models can be derived from first principles (Fick's laws, Bloch-Torrey equation), heuristic, or based on histological structures by including biophysical and geometric constraints. Finally, they can be tested using simulations, phantoms, and normal/abnormal tissues to evaluate their sensitivity and specificity.

In this study, we examine facets of this problem from the perspective of a linear, first-order diffusion process under the assumption that the diffusion coefficient will vary as the water explores tissue complexity at the subcellular, cellular and extracellular scales (< 1 μm, 1–5 μm, > 5 μm, respectively). We first examine the utility of what we call the varying diffusion curvature (VDC) model to describe normal and diseased human brain tissue, then consider how the contrast observed in white and gray matter reflects the porosity and tortuosity of packed beds of Sephadex beads, and also analyze simulations of muscle fiber bundles that are changed by removing fibers and by including increasing fiber wall permeability. This analysis illustrates the key characteristics of the VDC model that can be associated with water diffusion in heterogeneous materials.

2. Materials and methods

2.1. dMRI data collected from humans

Diffusion-weighted brain imaging was carried out on a healthy human volunteer (31-year-old female) and a glioma patient (41-year-old male with grade II glioma) under the approval by the institutional review board of the performing hospital. Axial images were acquired with a 3 Tesla General Electric MR750 scanner (General Electric Healthcare, Waukesha, Wisconsin) using a commercial 32-channel RF head coil. Multiple *b*-values using a single-shot echo planar imaging pulse sequence and Stejskal-Tanner diffusion gradients. The key data acquisition parameters for the healthy subject were: TR/TE = 4200/106 ms, slice thickness = 3 mm, inter-slice gap = 1 mm, $\Delta = 47$ ms, and $\delta = 32$ ms. Fourteen diffusion-weighted images (0_1, 20_1, 50_1, 100_1, 200_1, 400_1, 700_2, 1000_2, 1500_4, 2000_4, 2500_6, 3000_8, 3500_8, and 4000_8 s/mm^2, with the subscripts denoting the number of averages for the corresponding *b*-value) were acquired. The acquisition parameters for the glioma subject were: TR/TE = 4700/100 ms, slice thickness = 5 mm, slice spacing = 1.5 mm, $\Delta = 39$ ms, and $\delta = 32$ ms. Seventeen diffusion-weighted images (0_1, 20_1, 50_1, 100_1, 200_1, 400_1, 600_1, 800_1, 1000_1, 1200_1, 1600_1, 2000_2, 2400_2, 2800_2, 3200_4, 3600_4, and 4000_4 s/mm^2) were acquired. A field-of-view of 22 cm × 22 cm and matrix size of 256 × 256 were used for both acquisitions. At each *b*-value, the diffusion-weighting gradient was applied along the *x*, *y*, and *z*- axis, respectively, to obtain a trace-weighted image to minimize the effect of diffusion anisotropy.

2.2. dMRI data collected from gel bead phantoms

Sephadex™ is a commercial product (Sigma, St. Louis, MO) consisting of spherical beads fabricated as a network of chemically cross-linked dextrans. When fully hydrated it forms gels consisting of structurally heterogeneous polymer beads of uniform size that are commonly used for protein separation based on molecular size. Water moves easily into and out of the many small pores and channels of the gel while the much larger proteins are trapped and retained. In the absence of a bulk hydrostatic pressure, there is no net flow in the gel-water system, other than the translational displacement of water due to diffusion.

Seven different Sephadex™ gels were studied. Each gel is described by two numbers (e.g., G25–50); the first indicating the macromolecular exclusion limit associated with the pore network (in kDaltons), and the second specifying the maximum dry bead diameter (in microns). The first series of gels studied (G25–50, G25–80, G25–150, and G25–300) had the same internal structure (pores designed to retain relatively small proteins (< 25 kDaltons); but increasing bead diameters (from 50 to 300 μm). The second series of gels studied (G25–50, G50–50, G75–50 and G100–50) all had the same bead diameter, but with increasing internal pore sizes (designed to progressively retain proteins from 25 up to 100 kDaltons).

The gels were prepared by gently mixing the dry powder gels in excess distilled water at room temperature and allowed to swell and settle under the influence of gravity overnight. The next day the slurry was carefully poured into 5 mm diameter NMR tubes and sealed until used for the experiment (within 24 h). In each experiment, a complete series of hydrated gels were loaded into the NMR spectrometer.

The dMRI experiments were performed in the High Field MRI Facility at Pennsylvania State University. The gels were scanned using a Varian 14.1 Tesla (600 MHz) vertical bore micro-imaging spectrometer. The diffusion-weighted MRI data were acquired using a stimulated echo pulse sequence with Stejskal-Tanner diffusion gradients. The diffusion time Δ was varied from 27 to 200 ms and the pulse duration was fixed at $\delta = 5$ ms. The corresponding *b*-values for the experiments ranged from 100 up to 4000 s/mm^2. The amplitude of the diffusion encoding gradient, *G*, was varied from 0.01 to 0.4 T/m. Additional details are given in earlier work [9,10].

2.3. dMRI data synthetized using muscle fiber Monte-Carlo simulations

Many tissues (e.g., heart, brain white matter, muscle, cartilage, tendons, and ligaments) consist of nested fiber bundles, a feature exploited by dMRI. In this study we are not focused on the anisotropic structure of the biological material, but on aspects of sub-voxel structure that modulate diffusion. Monte-Carlo simulations are an established way to predict the effects on dMRI of changes in tissue composition and organization [11]. Here, we employ simulations developed for modeling muscle tissue fiber bundles to investigate the sensitivity of the VDC model to changes in fiber bundle size, number, and permeability.

White-matter fibers in the brain have radii on the order of 1–5 μm [12], which is compatible with diffusion times accessible in pulse gradient spin-echo (PGSE) or oscillating gradient spin-echo (OGSE) sequences. Muscle fibers are considerably larger: typically, 20–90 μm [13], requiring longer diffusion times for dMRI to probe. In addition, muscle tissue is hierarchical; consisting of bundle fibers that are in turn nested bundles of smaller fibers [14]. This structure restricts diffusion across a wide range of length scales from the macroscopic down to the nanoscale.

We used the Monte-Carlo simulation of diffusion in muscle tissue recently developed by Hall and Clark [15] to examine the VDC model for dMRI data synthesized across a wide range of gradient strengths and diffusion times. The simulations were performed by using CAMINO diffusion MRI toolkit [16]. The simulation parameters and the range of scan parameters used were the same as those described by Hall and

Clark [15]. A baseline tissue model derived from the histology of healthy tissue was compared with simulations developed for several scenarios that capture micro-structural changes that result from Duchenne muscular dystrophy (DMD) pathology, including: fiber atrophy, fiber removal, differences in fiber radius distribution, and changes in membrane permeability.

2.4. Varying diffusion curvature (VDC) model

The VDC model examined in the study is one of several presented in a recent paper [17] as a way to capture the change in ADC often observed in the dMRI signal decay. The VDC model is a simple generalization of the solution to Bloch-Torrey equation [18]. In the case of normal diffusion, the diffusion coefficient is a constant, and the acquired diffusion-weighted signal decays as $S(b) = S_0 \exp(-bD)$, where the effects of relaxation are collected in S_0 and D. Here, $S(b)$ depends on the local diffusion constant (D) and the shape and duration of the diffusion gradient waveforms, which are described by the following equation, for a general $G(t)$ gradient (Gauss/cm) applied in a single direction with total duration, T:

$$b = \gamma^2 \int_0^T \left(\int_0^t G(t')dt' \right)^2 dt. \tag{1}$$

For the Stejskal-Tanner pair of rectangular gradient pulses of amplitude (G), duration (δ) and separation (Δ) [19], Eq. (1) gives $b = (\gamma G\delta)^2(\Delta - \delta/3)$, where γ is the gyromagnetic ratio (42.57 MHz/Tesla for water protons) [20].

In the VDC model, we account for the change in slope of $\ln[S(b)]$ often observed at high b-values by allowing D to be function of b, $D(b)$, so that the dMRI signal can be expressed as:

$$S(b) = S_0 exp\left(- \int_0^b D(u)du \right), \tag{2}$$

where $D(b)$ is typically a monotonic decreasing function. Here we use $D(b) = D_0 exp(-bD_1)$, where D_0 in the VDC model is essentially the apparent diffusion coefficient (not the pure water diffusion constant), and D_1 is a measure of the tissue complexity. These parameters are obtained by fitting the dMRI data to the $S(b)$, which for this case is:

$$S(b) = S_0 exp\left[-\left(\frac{D_0}{D_1}\right)(1 - exp(-bD_1)) \right]. \tag{3}$$

This expression for $S(b)$ corresponds to the Gaussian case for $D_1 << D_0$, and the kurtosis model of diffusion signal decay for intermediate b-values (see Supplementary Material, and reference [17] for details).

Since the change in curvature of the $\ln[S(b)]$ decay curve corresponds to the onset of anomalous diffusion, we have used Eq. (3) and $C(b) = |S''(b)| / [1 + (S'(b))^2]^{3/2}$, where the primes indicate differentiation with respect to b, to obtain [21]:

$$\mathrm{C}(b) = \frac{D_0 S_0 \exp(-2bD_1) \exp\left(\frac{D_0(exp(-bD_1)-1)}{D_1}\right)(D_0 + D_1 \exp(bD_1))}{\left(D_0^2 S_0^2 \exp(-2bD_1) \exp\left(\frac{2D_0(exp(-bD_1)-1)}{D_1}\right) + 1\right)^{\frac{3}{2}}}. \tag{4}$$

As an example of the expected signal decay, $S(b)$, for the $D(b) = D_0 exp(-bD_1)$ decay example, we have plotted in Fig. 1a decay curves using Eq. (3) for four different values of D_0/D_1 with $S_0 = 1$ and $D_0 = 0.002 = 1/500\, mm^2/s$. The red curve is close to the standard single exponential decay, $S(b) = S_0 exp(-bD_0)$, which one gets in the limit $D_1 << D_0$ [17]. For hindered diffusion D_0 is reduced in value, just as occurs with the apparent diffusion coefficient, ADC = D_0/tortuosity, but the single exponential decay process is unchanged. The VDC model, however, also exhibits restricted diffusion (i.e., $D_1 = D_0$/restrictions) giving a final plateau corresponding to $D(b) \sim 0$ (narrow restrictions) and the constant value for $S(b) \sim S_0 exp(-D_0/D_1) = S_0 exp(-1) = 0.37 S_0$ shown in the blue curve in Fig. 1a. For progressively larger D_1 values (blue, black, green curves, respectively), $S(b)$ decays faster at low b-values and the final plateaus are higher; a behavior that mimics the trapped environment of restricted diffusion [22].

Intermediate values of b capture a decreasing slope of the diffusion-weighted signal decay $\ln[S(b)]$ in the same manner, and functional form, as expressed in the kurtosis model [5]. Here, a Taylor series expansion of Eq. (1) about $b = 0$ yields: $S(b) = exp(-bD_0)\, exp((D_1 D_0/2) b^2)$ [17,23]. In the intermediate range of b-values (500 to 1000 s/mm^2) the rate of change of the signal decay is greatest, and this feature is captured by Eq. (4). Fig. 1b shows plots of the curvatures for each $S(b)$ case plotted in Fig. 1a. For b-values > 200 s/mm^2, the larger the relative D_1 values, the smaller the curvature, which is evident in Fig.1a. Above $b = 2000$ s/mm^2, the $S(b)$ curve reaches a plateau and $C(b)$ approaches zero.

2.5. Data analysis and model fitting

The diffusion-weighted data was analyzed using Eq. (3) for all experiments. An iterative Levenberg-Marquardt method in Matlab (MathWorks, Inc., Natick, MA) was used to generate VDC model parameter maps, S_0, D_0, and D_1. For comparison, the conventional, *constant* apparent diffusion coefficient (ADC) values were also computed from a mono-exponential model given by $S = S_0\, exp(-b\, ADC)$, using b-values of 0 and 1000 s/mm^2, in a manner similar to that employed clinically. For images from the human subjects, the pixels with low signal-to-noise ratio (SNR) were filtered out by using a noise threshold that was set at $n + 2\sigma$, where n and σ are the mean and standard deviation of the noise in the background, respectively, as described in reference [24]. Pixels with intensity below the threshold were not included in the calculation. The diffusion images, S_{raw}, were also corrected for Rician noise using $S_{rc} = \sqrt{S_{raw}^2 - 2\sigma_n^2}$, where S_{rc} is the Rician noise corrected signal and σ_n is standard deviation of the real or imaginary components of the noise. The noise bias, $2\sigma_n^2$, was calculated as the average value of the magnitude squared signal of the background [25].

3. Results

3.1. Human subject experiments

Fig. 2 displays the diffusion-weighted signal intensity and the fitted curves obtained from the healthy human subject for three voxels selected from the region-of-interests (ROIs) of white matter (WM) from the corona radiata, gray matter (GM) from the caudate nucleus, and cerebral spinal fluid (CSF). We only showed one example, to identify the utility of the model. Our purpose here was not to examine brain tumor tissue, which includes edema, glial cells, necrosis, and hemorrhage, but to describe aspects of this model that can capture such complexity of both isotropic and anisotropic material. The good fitting quality of the VDC model for all ROIs can be clearly observed in Fig. 2a. Also shown in Fig. 2b is a fit of the same data to the mono-exponential model using the two b-values (0, 1000 mm^2/s) our clinical system employs for determining ADC. The mean and standard deviations for the estimated VDC model parameters, S_0, D_0, and D_1, computed over the corresponding ROIs selected from homogeneous structures are also given in Table 1. As expected, the normalized baseline parameter, S_0, was found to be close to one with a small standard deviation for all ROIs. The parameter, D_0, was found to be smaller in WM than GM reflecting the increased tissue heterogeneity and complexity arising due to the tightly packed axonal structures. On the other hand, the D_1 values in WM were higher than those in GM (Table 1). The largest D_0 and smallest D_1 were observed in CSF where the diffusion process is least hindered and restricted. This image contrast was preserved in the spatially resolved maps of D_0 and D_1 estimated from the healthy human subject data. The maps of D_0 and D_1 (as well as ADC and excess kurtosis

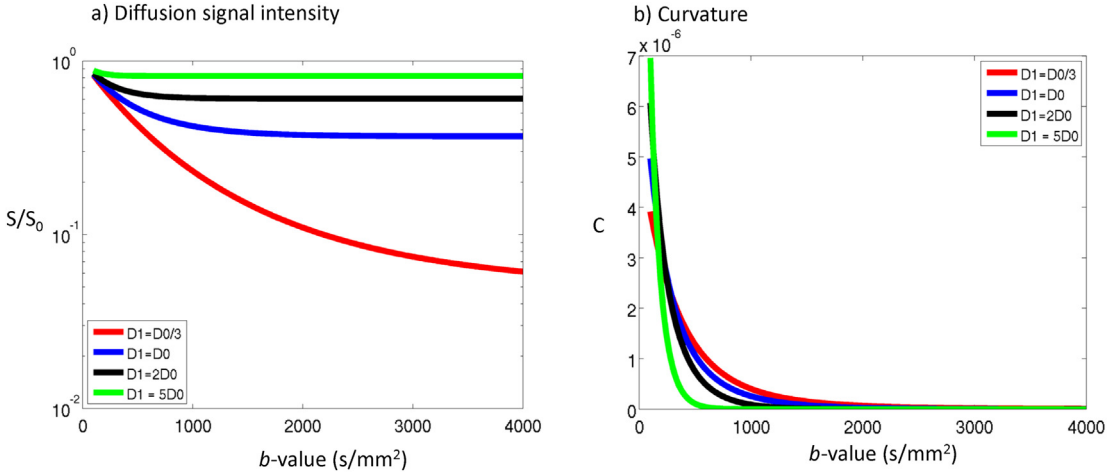

Fig. 1. Semi-logarithmic plot of signal decay (S/S_0 in a) versus *b*-value and the plot of the corresponding curvature (C in b) versus *b*-value computed using Eqs. (1) and (3), respectively for $S_0 = 1$ and $D_0 = 0.002\,\mathrm{mm^2/s}$ with individual cases of the ratio D_1/D_0 set to 1/3, 1, 2 and 5.

(K), for comparison) are given in Fig. 3a–d, respectively. While D_0 and ADC (Fig. 3a and c) provided similar contrast information, elevated values in some brain regions, such as the corona radiata can be clearly observed in D_1 (Fig. 3b) and K (Fig. 3d). D_1, ADC, and K gave different voxel values (higher in D_1 and K and lower in ADC) in the areas close to the edges of the ventricle than in the areas in the mid-CSF, possible due to partial volume averaging.

Fig. 4a–d show the spatially resolved maps of the VDC model parameters, D_0 and D_1, as well as ADC and K from a glioma patient. The tumor region was enhanced in the maps of D_0, ADC, and K with a similar image contrast as seen in Fig. 4a, c, and d. The parameter, D_1, on the other hand, produced lower values only in the solid tumor area within the tumor region. (black arrow in Fig. 4b). The higher values in the corona radiata can also be observed in D_1 and K maps.

3.2. Sephadex™ gel phantom experiments

Sephadex™ is a water permeable carbohydrate-based, size-exclusion gel filtration material formulated into spherical beads of different diameters (50, 80, 150 and 300 μm) with internal spaces that form a mesh designed to trap and release macromolecules below a fixed cutoff (25, 50, 75, and 100 kDaltons, in this study). Hence, for a set of 50-μm diameter beads, one expects the G100 beads to contain larger internal spaces (higher porosity) than the G 25 beads. Thus, the VDC model should exhibit a larger D_0/D_1 ratio for G100 than for G25. This behavior is evident in Fig. 5a for the G-sequence (100, 75, 50, 25: green, yellow, aqua and fuchsia). Clearly, the more complex, heterogeneous G25 Sephadex™ diffusion decay is fit by larger relative D_1 values, and a higher final plateau (consistent with more pronounced restricted diffusion in the relatively smaller internal spaces). The curvature plots (Fig. 5b) also capture this behavior with the faster decaying signals showing higher curvature values for the higher molecular weight cutoff G75 and G100 gel beads. For fixed δ and Δ, we expect greater restricted diffusion (lower D_1 values) for the smaller radius values (inverse relationship), where water cannot travel as far as that allowed by unrestricted Brownian motion. So, for beads with the same internal structure and of increasing diameters, the G25–50 beads should have the most restricted diffusion (higher plateau, lowest D_0/D_1 value), and G25–300 beads to have least restricted diffusion (lower plateau, higher D_0/D_1 value). Then, for beads of the same diameter (50 μm) and increasing molecular weight cutoff, the G25–50 beads would again have the most restricted diffusion, while the G100–50 beads would have the least restricted diffusion.

A similar pattern is exhibited in fits to the dMRI signal decay for the G 25 bead diameter sequence (50, 80, 150 and 300 μm: fuchsia, black, blue, red) in Fig. 5a. For this series of beads, the gels all have the same internal structure (G 25), but their diameters progressively increase. Assuming the same random packing density (and porosity), the 300-μm

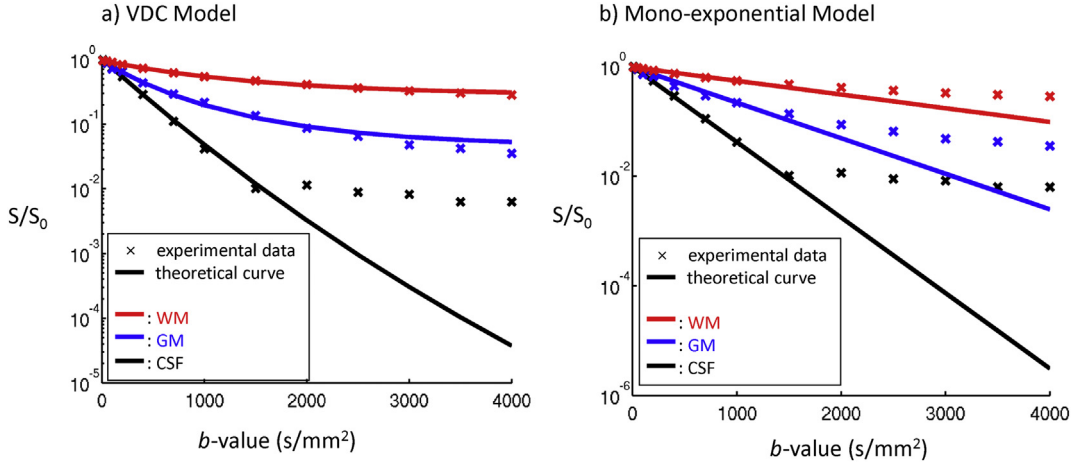

Fig. 2. Semi-logarithmic plot of signal decay (S/S_0) for the diffusion signal intensity for the data (cross marks) and fitted values (straight line) as a function of *b*-value from three representative ROIs selected from a healthy human subject. WM: white matter selected from corona radiata; GM: gray matter selected from caudate nucleus, CSF: cerebral spinal fluid. The VDC model was used on the left (a) and the mono-exponential model on the right (b).

Table 1
The descriptive statistics, sample mean and standard deviation, ($\bar{x} \pm \sigma$) of the VDC model parameters obtained from three representative ROIs in WM, GM, and CSF from a healthy human subject.

	S_0	D_0 (in mm^2/s)	D_1 (in mm^2/s)
WM	$0.98 \pm 0.5 \times 10^{-3}$	$0.81 \times 10^{-3} \pm 0.32 \times 10^{-8}$	$0.61 \times 10^{-3} \pm 0.69 \times 10^{-8}$
GM	$0.97 \pm 1.0 \times 10^{-3}$	$1.60 \times 10^{-3} \pm 0.10 \times 10^{-6}$	$0.48 \times 10^{-3} \pm 0.22 \times 10^{-7}$
CSF	$0.97 \pm 0.5 \times 10^{-3}$	$3.30 \times 10^{-3} \pm 0.20 \times 10^{-7}$	$0.15 \times 10^{-3} \pm 0.50 \times 10^{-8}$

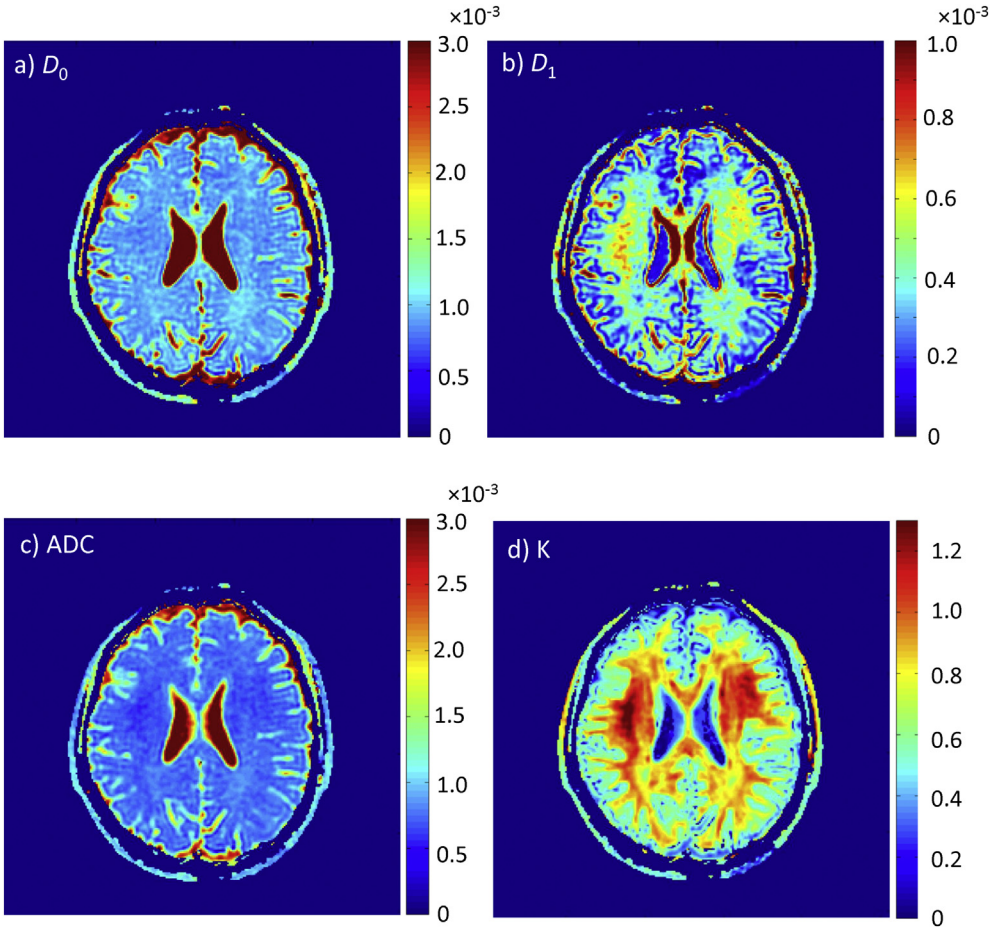

Fig. 3. Spatially resolved maps of D_0 in mm^2/s (in a), D_1 in mm^2/s (in b), ADC in mm^2/s (in c), and K (unitless, in d) obtained from a healthy human subject. These axial images were acquired at 3 Tesla with multiple *b*-values using a single-shot echo planar imaging pulse sequence and Stejskal-Tanner diffusion gradients. The specific imaging parameters (TR, TE, Δ, δ and b-values) are listed in the Materials and methods section.

beads would exhibit larger external spaces than the 50-μm beads. This can be expected to enhance diffusion and increase the D_0/D_1 ratio, corresponding to a more pronounced diffusion weighted signal decay with increasing bead diameter. This behavior evident in the fuchsia, black, blue, and red $S(b)/S_0$ curves in Fig. 5a and is displayed in the curvature plots (Fig. 5b).

The VDC model was also fit to dMRI decay curves acquired using the Stejskal-Tanner diffusion pulse sequence for three values of small delta (δ = 3, 5 and 7 ms) and six values of large delta (Δ = 25, 50, 75, 100, 150 and 200 ms). Fig. 6a and b show how the D_0 and D_1 values change with Δ for the case of δ = 3 ms. In the D_0 data (Fig. 6a) two trends are evident. First, the D_0 values are constant for the fixed diameter sequence of G values; but decrease for the changing diameter sequence of G 25 beads. This reflects the sensitivity of the bulk diffusion D_0 to the changing volume outside of the bead, not to changes in the internal bead structure. For the D_1 data (Fig. 6b) an opposite trend is observed; the D_1 values increase with Δ for the fixed diameter sequence of G values, while it is relatively constant for the changing diameter sequence of G 25 beads. Thus, here D_1 is more sensitive to the internal structure of the beads. The same general behavior was observed for the range of δ values studied. Thus, in applying the VDC model to this family of Sephadex™ beads, we see that distinct features of the gel structure (bead diameters) and composition (bead crosslinks) are captured in the D_0 and D_1 values, respectively. In addition, fine tuning of this sensitivity can be modulated by varying δ, Δ, and *b*-value, while using the curvature plots to isolate the most sensitive regions for data collection.

3.3. Muscle fiber simulation comparisons

In this section we apply the VDC model to diffusion Monte-Carlo simulation results for muscle tissue published by Hall and Clark [15]. Fitting simulation data is an intermediate step between the analysis of gel phantoms of packed Sephadex™ beads and the dMRI study of human brain tissue. The gels are heterogeneous and isotropic, while the muscle simulations are heterogeneous and anisotropic on multiple length scales, so the former is similar to gray matter, while the latter corresponds in some features to white matter. The nested cylindrical fiber model of muscle used by Hall and Clark consists of hierarchical assemblies of smaller fibers (Fig. 2 in Hall and Clark [15]), which provides a natural way to modify the relative amount of hindered and restricted diffusion. The focus of the Hall and Clark study was on

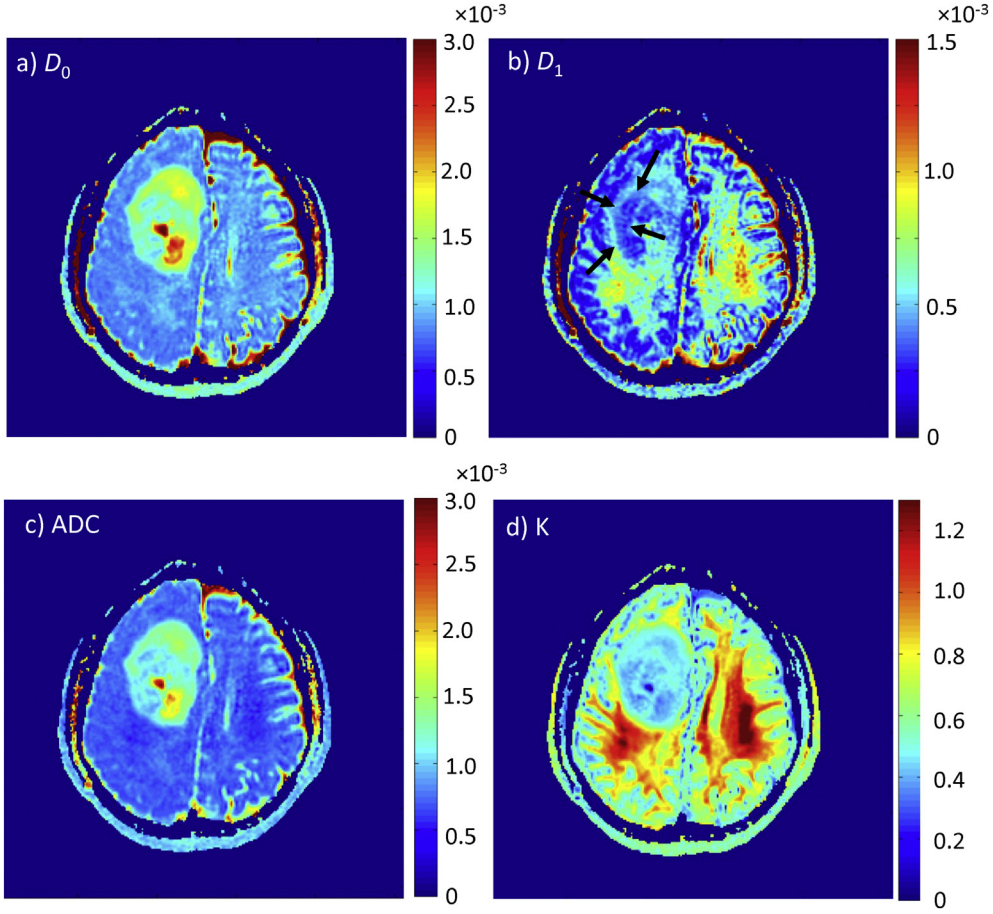

Fig. 4. Spatially resolved maps of D_0 in mm^2/s (in a), D_1 in mm^2/s (in b), ADC in mm^2/s (in c), and K (unitless, in d) obtained from a glioma patient. These axial images were acquired at 3 Tesla with multiple *b*-values using a single-shot echo planar imaging pulse sequence and Stejskal-Tanner diffusion gradients. The black arrows (in b) point to the solid tumor area within the tumor region. The specific imaging parameters (TR, TE, Δ, δ and b-values) are listed in the Materials and methods section.

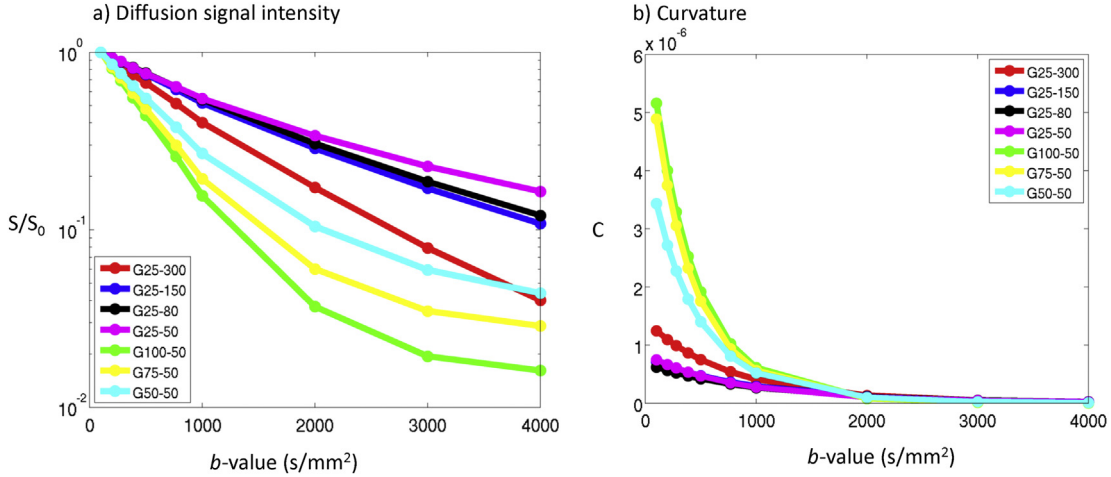

Fig. 5. Semi-logarithmic plot of the decay in the diffusion signal intensity (S/S_0 in a) and the plots of curvature (C in b) as a function of *b*-value for gels G25–300, G25–150, G25–80, G25–50 with the same internal structure, but with decreasing bead diameter from 300 to 50 μm; and for G100–50, G70–50, and G50–50, with the same bead diameter, but with increasing internal pore sizes. The diffusion time parameters were set to δ = 5 ms and Δ = 75 ms for this experiment.

determining the sensitivity of dMRI to changes in the structure (muscle fiber loss, muscle fiber atrophy) and composition (cell wall permeability, fiber diameter distribution) of muscle fibers; changes of the type that are known to occur in DMD. Here, we fit only a subset of the Hall and Clark data – as a function of *b*-value – to investigate the sensitivity of the VDC model parameters (S_0, D_0, and D_1) to atrophy due to shrinkage of internal muscle fiber diameters, increasing membrane permeability, and changes in the fiber diameter distribution (normal muscle versus DMD).

Changes in fiber permeability were simulated by allowing a small fraction of the water undergoing Brownian motion within each fiber to transition across fiber membranes rather than be scattered by them. Given sufficient diffusion time, the water will encounter and be reflected by the surrounding fiber wall (in the absence of permeability) leading to a reduction the apparent diffusion coefficient (restricted diffusion) and a plateau in the signal decay curve, $S(b)$ at high *b*-values. Increasing membrane permeability (reduces restricted diffusion) permitting some spins to transition, which removes the hard minimum on the plateau and as such has a large effect on the signal at high b-value. This effect is illustrated by the data plotted in Fig. 7 for a dMRI

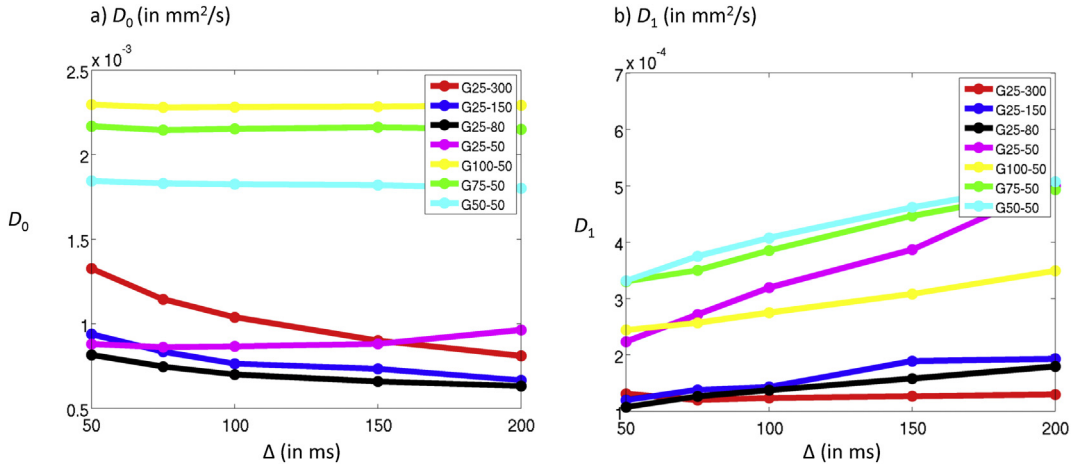

Fig. 6. Estimated values of the varying diffusion curvature (VDC) model parameters, D_0 in mm^2/s (in a) and D_1 in mm^2/s (in b), as a function of pulse separation, Δ, for gels G25–300, G25–150, G25–80, G25–50 with the same internal structure, but with decreasing bead diameter from 300 to 50 μm, and for G100–50, G70–50, and G50–50, with the same bead diameter, but with increasing internal pore sizes. The pulse width, δ, was set to 3 ms for this experiment.

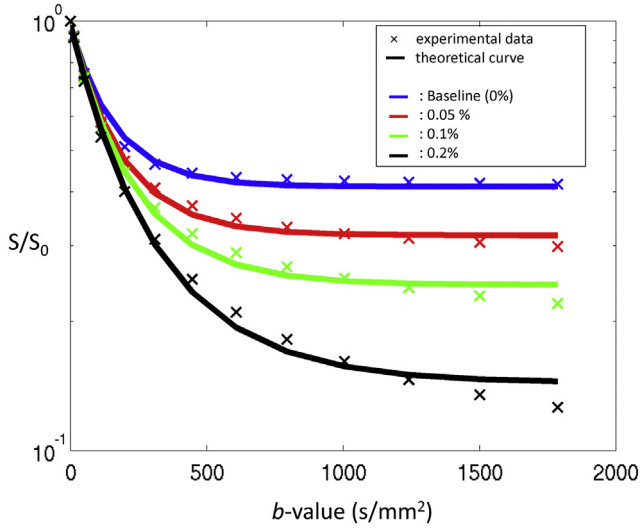

Fig. 7. Semi-logarithmic plots of the simulated (cross mark) and fitted (straight line) diffusion signal intensity (S/S_0) as a function of *b*-value for baseline, and for fiber bundle substrates with 0.05%, 0.1%, and 0.2% permeability.

Table 2
The VDC model parameter values and asymptote obtained from different simulation scenarios: baseline; 0.05%, 0.1%, and 0.2% permeability change; 5%, 10%, and 20% atrophy change; and fiber radius distribution change based on Mdx mouse model.

	S_0	D_0 (in mm^2/s)	D_1 (in mm^2/s)	Asymptote
Baseline	0.97	5.2	6.0	0.41
Perm (0.05%)	0.99	5.9	5.2	0.32
Perm (0.1%)	0.98	5.9	4.2	0.24
Perm (0.2%)	0.98	5.9	3.1	0.14
Atrophy (5%)	0.96	5.8	6.0	0.36
Atrophy (10%)	0.95	6.0	5.7	0.33
Atrophy (20%)	0.92	6.0	4.7	0.26
Mdx	0.97	4.9	6.0	0.43

simulation with (0, 0.05, 0.1 and 0.2%) permeability. In these plots the solid curves are the fits to $S(b)/S_0$ using Eq. (3), and the crosses are the Monte-Carlo simulation results. The calculated VDC model parameters are listed in Table 2 for convenience. The principal effect of increasing fiber wall permeability is on D_1, not D_0, which is consistent with their respective roles in describing restricted and hindered diffusion, and the final asymptote is a plateau that is given by $S_0 exp(-D_0/D_1)$.

Atrophy due to fiber shrinkage was simulated by a 5, 10, and 20% reduction in the internal muscle fiber diameters. The smaller fiber cross sections are therefore more quickly explored – greater restricted diffusion – yielding lower plateaus. This effect is illustrated by the data plotted in Fig. 8 for a dMRI simulation with (5, 10 and 20% reduction of internal fiber diameters) giving corresponding reductions of the plateaus of 9.4, 18.6 and 34.7% from the control. Again, the primary VDC model parameter affected was D_1. These data are also listed in Table 2.

Changes in the fiber radius distribution are known to occur in DMD [15]. However, altering the distribution (control Gamma and Mdx mouse model of DMD) does not have as large an effect on the $S(b)$ decay curve or the VDC model of the simulation data. The results for the Gamma distribution baseline and the Mdx cases show that D_0 was more sensitive than D_1 (hindered diffusion > restricted diffusion). These preliminary results are also listed in Table 2.

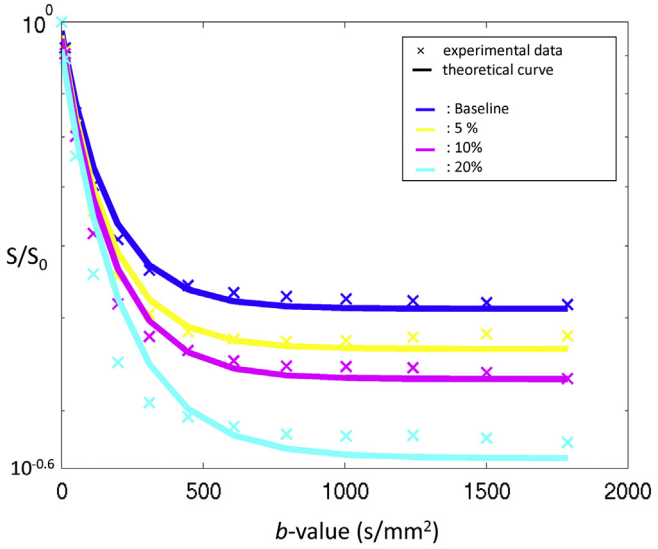

Fig. 8. Semi-logarithmic plots of the simulated (cross mark) and fitted (straight line) diffusion signal intensity (S/S_0) as a function of *b*-value for baseline, and for fiber bundle substrates with 5, 10, and 20% atrophy in the internal cylinder radius.

4. Discussion[1]

The impetus to glean diagnostic information from dMRI data reflects the tension between advancing technology and the goals of personalized medicine. Fast, whole-body, and high-resolution imaging empowers the search for biomarkers to identify, stage, and classify tumors (e.g., breast, prostate), and neurodegenerative disease (Alzheimer's, Huntington's, etc.). Patients want earlier warnings and physicians want complete tissue characterization; aspirations that place the radiologist and MR researcher on a quest to correlate image 'features' with changes in tissues arising due to developing pathology.

Unlike X-rays or ultrasound where tissue structure and composition directly affect the absorption, scattering and reflection of energy, MRI has two indirect, or hidden, layers of interaction (induced spin polarization, deduced magnetization dynamics) that modulate the detected signal intensity (amplitude and phase) and the derived image parameters (e.g., relaxation time, diffusion coefficient, conductivity, stiffness). Both intervening processes involve models of how magnetic and radiofrequency fields affect and are affected by the time and space evolution of magnetic resonance phenomena in tissues (Bloch and Bloch-Torrey equations) [18,20,22]. Interrogation of a particular tissue feature using relaxation or diffusion requires specific pulse sequences (e.g., Hahn spin echo for T_2, or Stejskal-Tanner diffusion encoding), but interpretation of the collected data involves assumptions (compartmentalization, course graining or mean field theory) of sub-voxel tissue complexity that affect the extraction of a meaningful biomarker for tissue structure or composition [27,28].

Advances in dMRI proceed as a two-step process with improved diffusion-weighted imaging sequences employing improved RF and gradient hardware to collect the arrays of data needed to analyze the multi-compartment models [7,8] (e.g., neurite orientation dispersion and density imaging, and composite hindered and restricted diffusion) of sub-voxel tissue structure. This imaging 'arms race' has recently been called into question [27] with respect to its added value in answering the questions raised by physicians and patients. The goal of this paper was not to delve deeper into the tissue or the techniques, but to consider the dilemma from the opposite perspective; to select one robust signal characteristic and to project it back to a simple heuristic model. Hence, we have focused on the decrease in the ADC with time (or b-value) and fit dMRI data using the VDC model using the simple exponential decay [15], $D(b) = D_0 exp(-bD_1)$.

In general, this model captures aspects of hindered and restricted diffusion in D_0 and D_1, respectively, where the D_0 for homogeneous materials is equivalent to the ADC or the intrinsic free diffusion constant divided by the tortuosity (hindered diffusion), and D_1 captures the effects of reflections at cell or membrane boundaries (restricted diffusion). As shown in a previous publication [17], this exponential decay model is only one option, but it does encode the commonly observed flattening out of the $\ln[S(b)]$ signal decay as a function of b-value in white matter and in muscle tissue (Fig. 3). Operationally, at intermediate b-values, the exponential model is equivalent to the kurtosis model [5]; and expresses a multi-compartment sum of regular exponential behavior in $S(b)$ over the entire range of b-values [17]. In summary, D_0 is similar to ADC, as expected, having lower values in more complex tissue structures (lowest in WM, intermediate value in GM, and highest in CSF). D_1 is different from D_0 (hence may be interesting as a biomarker) in that a reverse pattern is observed. Although we do not know exactly what D_1 reflects, this outcome is consistent with Sephadex results in Fig. 6b. where the more complex, heterogeneous G25 Sephadex™ diffusion decay is fit by larger relative D_1 values, while here, we have higher D_1 values that are correlated with more restricted structures such as those in WM.

In this paper, we applied the VDC model to dMRI data from three heterogeneous materials (Sephadex™ gel phantoms, muscle fiber simulations, and human brain tissue). Sephadex™ gel phantoms have been well studied using dMRI [9,10] because their diameter, porosity, and tortuosity can be adjusted allowing the researcher to investigate changes in $S(b)$ with bead diameter and the size of the internal bead spaces. Fits of $S(b)$ data to families of Sephadex™ gel beads using the VDC model (S_0, D_0, D_1) captures the plateau seen at high b-values, demonstrates a good correlation between bead heterogeneity and D_1, and illustrates the effect of bead packing on D_0. Monte-Carlo, muscle fiber simulations also are a useful tool for correlating changes in fiber diameter, packing and permeability with dMRI signals. Ideally, one can use simulations to optimize the diffusion pulse sequence parameters to highlight changes in the model parameters that correspond to disease progression (muscle atrophy due to fiber loss or changes in the fiber diameter distribution). We fit the VDC model to simulated $S(b)$ data and found that the D_1 parameter (but not D_0) was most sensitive to changes in fiber permeability and to a reduction in fiber diameter. Conversely, D_0 was more sensitive than D_1 to changes in fiber diameter distribution. dMRI is often used to stage and monitor brain diseases, so we also used the VDC model to fit $S(b)$ data from a normal volunteer and from a glioma patient. The D_0 maps for white and gray matter in the brain of the volunteer displayed similar contrast to the ADC fits, while the D_1 maps for white matter trace images showed contrast that appears to display some of the features identified by kurtosis imaging [1]. In our model the D_1, like excess kurtosis, K, is a way to capture additional information from tissue regions that exhibit restricted diffusion. Nevertheless, from this single clinical case, we cannot elaborate on how D_1 might be helpful in tumor staging, but we are pursuing this question with our clinical colleagues. For the glioma patient, again we found good correspondence between the D_0 maps and ADC in the brain parenchyma and in the tumor. The D_1 map for the tumor showed less contrast; but displayed several white matter regions with good to excellent contrast. These results are illustrative only; and will be pursued in future studies with groups of patients to substantiate the observations in this study. Taken together, the gel phantom, muscle simulations, and clinical MRI results display the capabilities of the VDC model to identify specific features of heterogeneous materials, features that reflect sub-voxel structure and composition.

Beyond their utility, another reason to pursue simple models for diffusion in heterogeneous materials is that even for the simplest diffusion gradient pulse sequences and signal attenuation models – the short pulse approximation (SPA) and the Gaussian phase approximation (GPA) – the resulting signal attenuation conflates b-value and diffusion coefficient, D, as $S/S_0 = exp[-bD]$, where b is a function of the diffusion pulse sequence and D is a voxel average. Unravelling the contributions of sub-voxel contributions to D from the corresponding changes in $b(G, \Delta, \delta)$ is at best difficult and at worse, impossible because there are usually more than one configuration of intra- and extra-cellular sub-voxel compartments that will give the same bD product, that is, the solution is not uniquely described by a single sub-voxel structure. This structural degeneracy is a shortcoming in all compartmental models; and is often compounded by the assumption that the water does not exchange between compartments. Such reservations should give pause to modeling recipes that try to associate tissue histology with dMRI and harken back to Kac's classic paper, 'Can One Hear the Shape of a Drum?' [29].

In addition, the $D(b)$ model of anomalous diffusion [17] involves two distinct aspects of the normal (Gaussian) model of diffusion: one in time and one in space. The Gaussian model of dMRI uses the b-value as the independent variable, but this term is the scaled product of q^2 and t, where q is the Fourier transform of the underlying diffusion process [22] ($q = (1/2\pi)\ (\gamma G\delta)^2$), and t is the diffusion time ($t = (\Delta - \delta/3)$). Ideally, one should probe $S(b)$ at many points in (q, t) space using experiments [30,31] or simulations [15]. Alternatively, we could extend D to be function of space, $D(x)$, or time, $D(t)$, or both time and space, D

[1] *Modeling is the direct object of the measurement here.*
(with acknowledgment to Mr. Charles Lamb, page 245 of [26])

(x,t). As is the case when using fractional order space and time derivatives to capture nonlocality and memory [32], using $D(x,t)$ is an a priori choice that modellers must make to describe measurements on complex materials.

Time and distance are interconnected for both normal and anomalous diffusion, so the different terms in the diffusion models, can represent subcellular, cellular and extracellular (< 1 μm, 1–10 μm, > 10 μm) compartments [33,34]. Ideally, each term should be associated with a different set of compartments and boundary conditions. If we knew the physical mechanism governing the apparent reduction in $D(b)$ that occurs in tissue, then we could compute a forward model, but this sub-voxel information is not observable in normal tissues using dMRI; and is not known for diseased brain tissue. Based on our previous work [35,36], and the work of others [37], fractional calculus models also have the potential to distinguish the substructure in complex materials (e.g., in viscoelasticity, dielectrics, and electrochemistry). Specifically, the recent book by Evangelista and Lenzi [38] describes how power-law models and fractional calculus can provide links between material structure and anomalous diffusion. The focus here, however, is on a $D(b)$ model of anomalous diffusion, which does not use fractional calculus.

5. Conclusions

The VDC model can capture features of tissue complexity (porosity, tortuosity, atrophy, permeability) in the diffusion-weighted MR signal decay that reflect changes in $D(b)$ due to sub-voxel tissue structure and composition. The VDC model parameter D_0 corresponds to hindered diffusion (changes in porosity and tortuosity, in a manner similar to the tissue ADC), while the D_1 parameter is more sensitive to restricted diffusion and permeability. The simplicity of this model and the expanding capabilities of diffusion gradients (higher b-values) on clinical imaging systems offer the promise of its easy implementation and future use in the detection, monitoring and management of disease.

Acknowledgements

A portion of this work was presented at the 14th International Bologna Conference on Magnetic Resonance in Porous Media, held February 18-22, 2018 at the University of Florida, Gainesville, FL. R. Magin, M. Karaman and J. Zhou wish to acknowledge support from the National Institutes of Health through Grant No. R01EB026716 and Grant No. 1S10RR028898. M. Hall was supported by a grant from the Biomedical Research Centre of the Great Ormand Street Hospital and by the National Physical Laboratory, Teddington, UK. The authors also wish to acknowledge the assistance of Thomas Neuberger in the collection of the Sephadex™ data at the Center for Magnetic Resonance Imaging at Pennsylvania University, and assistance of Dr. Jiaxuan Zhang for obtaining the patient data at Tongji Hospital, Huazhong University of Science and Technology in China.

Supplementary material

Supplementary data to this article can be found online at https://doi.org/10.1016/j.mri.2018.09.034.

References

[1] Le Bihan D. Looking into the functional archetecture of the brain with diffusion MRI. Nat Rev Neurosci 2003;4(6):469–80.
[2] Maier SE, Sun Y, Mulkern RV. Diffusion imaging of brain tumors. NMR Biomed 2010;23(7):849–64.
[3] Kono K, Inoue Y, Nakayama K, Shakudo M, Morino M, Ohata K, et al. The role of diffusion-weighted imaging in patients with brain tumors. Am J Neuroradiol 2001;22(6):1081–8.
[4] Yamasaki F, Kurisu K, Satoh K, Arita K, Sugiyama K, Ohtaki M, et al. Apparent diffusion coefficient of human brain tumors at MR imaging. Radiology 2005;235:985–91.
[5] Jensen JH, Helpern JA, Ramani A, Lu H, Kaczynski K. Diffusional kurtosis imaging: the quantification of non-Gaussian water diffusion by means of magnetic resonance imaging. Magn Reson Med 2005;53:1432–40.
[6] Novikov DS, Fieremans E, Jensen JH, Helpern JA. Random walks with barriers. Nat Phys 2011;7(6):508–14.
[7] Zhang H, Schneider T, Wheeler-Kingshott CA, Alexander DC. NODDI: practical in vivo neurite orientation dispersion and density imaging of the human brain. Neuroimage 2012;61(4):1000–16.
[8] Assaf Y, Freidlin RZ, Rohde GK, Basser PJ. New modeling and experimental framework to characterize hindered and restricted water diffusion in brain white matter. Magn Reson Med 2004;52(5):965–78.
[9] Liang Y, Chen W, Akpa BS, Neuberger T, Webb AG, Magin RL. Using spectral and cumulative spectral entropy to classify anomalous diffusion in Sephadex™ gels. Comput Math Appl 2017;73(5):765–74.
[10] Magin RL, Akpa BS, Neuberger T, Webb AG. Fractional order analysis of Sephadex gel structures: NMR measurements reflecting anomalous diffusion. Commun Nonlinear Sci Numer Simul 2011;16(12):4581–7.
[11] Alexander DC, Hubbard PL, Hall MG, Moore EA, Ptito M, Parker GJM, et al. Orientationally invariant indices of axon diameter and density from diffusion MRI. Neuroimage 2010;52(4):1374–89.
[12] Aboitiz F, Scheibel a B, Fisher RS, Zaidel E. Fiber composition of the human corpus callosum. Brain Res 1992;598(1–2):143–53.
[13] Hooijmans MT, Damon BM, Froeling M, Versluis MJ, Burakiewicz J, Verschuuren JJGM, et al. Evaluation of skeletal muscle DTI in patients with duchenne muscular dystrophy. NMR Biomed 2015;28(11):1589–97.
[14] Saladin K, Miller L. Anatomy & physiology. 3rd ed. New York: Watnik; 2010.
[15] Hall MG, Clark CA. Diffusion in hierarchical systems: a simulation study in models of healthy and diseased muscle tissue. Magn Reson Med 2016;00:1–12.
[16] Hall MG, Alexander DC. Convergence and parameter choice for Monte-Carlo simulations of diffusion MRI. IEEE Trans Med Imaging 2009;28(9):1354–64.
[17] Magin RL. Models of diffusion signal decay in magnetic resonance imaging: capturing complexity. Concepts Magn Reson Part A Bridg Educ Res 2016;45A(4).
[18] Haacke E, Brown R, Thompson M, Venkatesan R. Magnetic resonance imaging: physical principles and sequence design. New York: Wiley-Liss; 1999.
[19] Stejskal EO, Tanner JE. Spin diffusion measurements: spin echoes in the presence of a time-dependent field gradient. J Chem Phys 1965;42(1):288–92.
[20] Jones DK. Diffusion MRI theory, methods, and applications. 2010.
[21] Anton H. Calculus with analytic geometry. New York: John Wiley and Sons; 1980.
[22] Callaghan PT. Translational dynamics and magnetic resonance: principles of pulsed gradient spin echo NMR. Oxford: Oxford Univ. Press; 2011.
[23] Jensen JH, Helpern JA. MRI quantification of non-Gaussian water diffusion by kurtosis analysis. NMR Biomed 2010;23(7):698–710.
[24] Zhou XJ, Gao Q, Abdullah O, Magin RL. Studies of anomalous diffusion in the human brain using fractional order calculus. Magn Reson Med 2010;63:562–9.
[25] Miller AJ, Joseph PM. The use of power images to perform quantitative analysis on low SNR MR images. Magn Reson Imaging 1993;11(7):1051–6.
[26] Lamb C. Morpurgo JE, editor. Selected writings. New York: Routledge; 2003.
[27] Novikov DS, Kiselev VG, Jespersen SN. On modeling. Magn Reson Med 2018;79(6):3172–93.
[28] Valiullin R, editor. Diffusion NMR of confined systems: fluid transport in porous solids and heterogeneous materials. The Royal Society of Chemistry; 2017.
[29] Kac M. Can one hear the shape of a drum? Am Math Mon 1966;73(4(2)):1–23.
[30] Ingo C, Magin RL, Colon-Perez L, Triplett W, Mareci TH. On random walks and entropy in diffusion-weighted magnetic resonance imaging studies of neural tissue. Magn Reson Med 2014;71(2):617–27.
[31] Magin RL, Ingo C, Colon-Perez L, Triplett W, Mareci TH. Characterization of anomalous diffusion in porous biological tissues using fractional order derivatives and entropy. Microporous Mesoporous Mater 2013;178:39–43.
[32] Magin RL, Abdullah O, Baleanu D, Zhou XJ. Anomalous diffusion expressed through fractional order differential operators in the Bloch-Torrey equation. J Magn Reson Imaging 2008;190:255–70.
[33] Grebenkov DS. From the microstructure to diffusion NMR, and back. In: Valiullin R, editor. Diffusion NMR of confined systems: fluid transport in porous solids and heterogeneous materials. The Royal Society of Chemistry; 2017.
[34] Grinberg F, Farrher F, Shah NJ. Diffusion magnetic resonance imaging in brain tissue. In: Valiullin R, editor. Diffusion NMR of confined systems: fluid transport in porous solids and heterogeneous materials. The Royal Society of Chemistry; 2017.
[35] Sui Y, He W, Damen FW, Wanamaker C, Li Y, Zhou XJ. Differentiation of low- and high-grade pediatric brain tumors with high b-value diffusion weighted MR imaging and a fractional order calculus model. Radiology 2015;277(2):489–96.
[36] Karaman MM, Sui Y, Wang H, Magin RL, Li Y, Zhou XJ. Differentiating low- and high-grade pediatric brain tumors using a continuous-time random-walk diffusion model at high b-values. Magn Reson Med 2016;76(4):1149–57.
[37] Klages R, Radons G, Sokolov IM, editors. Anomalous transport: foundations and applications. Weinheim: Wiley-VCH; 2008.
[38] Evangelista LR, Lenzi EK. Fractional diffusion equations and anomalous diffusion. Cambridge, UK: Cambridge Univ. Press; 2018.